Eur. Phys. J. D **41**, 221–227 (2007)
DOI: 10.1140/epjd/e2006-00242-8

**THE EUROPEAN
PHYSICAL JOURNAL D**

Open-channel fluorescence imaging of atoms in high-gradient magnetic fields

R.R. Mhaskar[a], S.E. Olson, and G. Raithel

FOCUS Center, Physics Department, University of Michigan, 450 Church Street, Ann Arbor, Michigan 48109-1120, USA

Received 18 March 2006 / Received in final form 20 June 2006

Abstract. A method of imaging distributions of cold atoms under the presence of large trapping-field-induced level shifts is investigated. By utilizing a probe laser tuned to an open transition, the fluorescence yield per atom is largely fixed throughout the trap volume, independent of the trapping field. This enables a reliable conversion of fluorescence images into atomic-density profiles. The method is applied to measure distributions of ^{87}Rb atoms in a high-gradient (2.7 kG/cm) magnetic atom guide. We characterize the parameters for which the open-channel imaging method performs best. Results of quantum Monte Carlo simulations verify the underlying assumptions of the method.

PACS. 32.50.+d Fluorescence, phosphorescence (including quenching) – 32.80.-t Photon interactions with atoms

1 Introduction

While the development of a wide variety of traps for atoms [1] and molecules [2] has spanned the past few decades, imaging has been the key to observing and investigating physical phenomena in trapped-particle clouds. The most common method of imaging distributions of cold atoms involves illuminating the trap region with a monochromatic probe laser tuned to a closed-channel "cycling" transition and detecting the ensuing fluorescence or measuring the probe absorption. Closed-channel imaging leads to a high photon yield per atom and thus a high signal-to-noise ratio of the images. In high-gradient traps, the fluorescence rate per atom is highly dependent on position due to spatial variations of Zeeman- and/or Stark-shifts throughout the sample, variations of the angle between the laser polarization and the trapping fields, and optical pumping among magnetic sublevels. In this case, the processing of fluorescence images into actual particle density distributions requires very detailed modeling. Hence, magnetic, electric, and optical trapping fields are typically switched off during the fluorescence or absorption imaging. By switching the fields off, the spatial variation of the fluorescence rate is avoided, resulting in a uniform photon yield per atom and reliable conversion of fluorescence images into density distributions.

In some systems, switching the trapping fields off in order to perform distribution measurements may not be possible or even desirable. This is the case, for example, in magnetic atom traps where ferromagnetic materials are used [3,4]. In experiments involving magnetic traps with high field gradients, such as achieved in atom-chip experiments [5] or high-gradient atomic guides [6], the process of switching fields can involve switching large currents. This leads to rapid thermal cycling effects that may cause micro-leaks to appear at the vacuum feedthroughs [7] and also to transients in the current loop due to high inductance. In other cases, it is desired to measure the steady-state distribution of cold atoms in systems with an equilibration time in the range of several seconds or more, such as a scheme shown to load a Ioffe-Pritchard trap with chromium atoms [8] as well as continuously loaded, long atom guides [7,6]. In such cases, switching the fields off in order to acquire an image will necessitate a long waiting time for the system to become ready again for the next image to be taken. Consequently, an unacceptably low measurement repetition rate may result. Therefore, a robust imaging method is needed that delivers true representations of cold-atom distributions with the trapping fields left on.

At least two methods exist from which a signal that is directly proportional to the density of the sample can be delivered. The first, phase-contrast imaging (a non-destructive scheme), allows one to measure the change of the index of refraction for far-off-resonant light propagating through an atomic sample that is optically dense at resonant frequencies. The disadvantage of this method lies in the requirement to have atomic samples of very high density, which in many cases are not available. A second method relies on the optical pumping of atoms using an open transition. This open-channel imaging method is occasionally used to measure the total atom number

---

[a] e-mail: `rmhaskar@umich.edu`

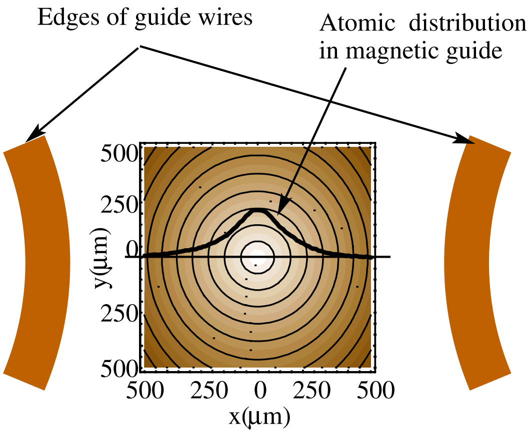

Fig. 1. Contour plot of the magnetic field of the atom guide vs. position (x, y). The contour lines show the transverse magnetic trapping field established by two parallel wires carrying parallel currents of 300 A. This establishes a field gradient of 2.7 kG/cm in the vicinity of the minimum of the magnetic-field strength. The separation between adjacent contour lines is 20 G. Typical distributions of trapped atoms (overlaid curve) extend into regions with magnetic fields on the order of 50 G, corresponding to Zeeman shifts on the order of 70 MHz.

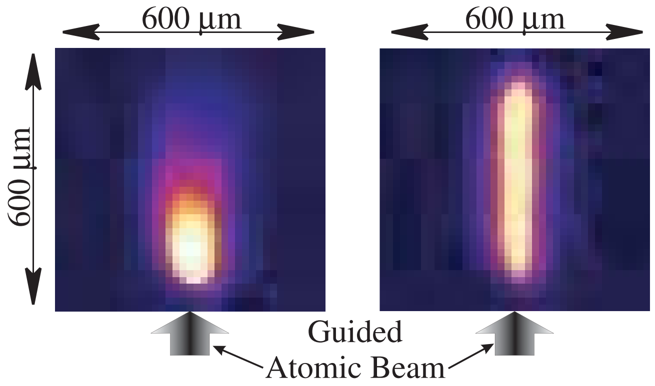

Fig. 2. (Color online) (Left) Fluorescence image of a distorted atomic beam obtained with a continuous probe. (Right) Non-distorted atomic beam imaged via strobed probe pulses of 20 μs duration and 1 ms separation.

in optically thick samples [9,10]. As discussed in this paper, in certain cases open-channel probing also is the best method to characterize non-optically-thick magnetically guided atomic beams. Recently, Lahaye et al. [7] have used open-channel absorption measurements to obtain profiles and fluxes of magnetically guided atomic beams, and open-channel fluorescence has been imaged to obtain pictures of such beams [6].

In this paper, we characterize the performance of the open-channel cold-atom imaging method in cases where Zeeman shifts change significantly through the detection region. The method yields accurate atomic density distributions and should be applicable to other trapping situations. We believe that this method could also be useful to image trapped molecules (which do not offer closed optical transitions).

2 Magnetic-trapping device

The magnetic-trapping setup used to demonstrate open-channel imaging consists of a high-gradient magnetic guide with a two-wire geometry in which ^{87}Rb atoms are guided (for a detailed description, see [6]). In this setup, approximately parallel water-cooled copper tubes of about 2 m length, carrying parallel currents of 300 A, create a linear magnetic guide with a magnetic gradient as large as 2.7 kG/cm at the guide axis. The cross-section of the trapping magnetic field is shown in Figure 1.

To fill the guide with cold atoms, a primary, unguided, cold atomic beam generated by a pyramidal magneto-optic trap (PMOT) [11,12] intersects with the atom guide. A so-called moving-MOT (MMOT) [13,14] then transfers the atoms from the primary atomic beam into the magnetic guide. The MMOT employs cooling lasers ~16 MHz red-detuned to the 5S$_{1/2}$ $F = 2 \leftrightarrow$ 5P$_{3/2}$ $F' = 3$ cycling transition of ^{87}Rb. The MMOT collects atoms from the primary atomic beam, cools them onto the atom-guide axis, and launches them into the atom guide with a velocity of 2.5 m/s parallel to the guide axis. To avoid trap-loss due to the scattering of MMOT stray light, the injected atoms are optically pumped into the $|F = 1, m_{\mathrm{F}} = -1\rangle$ ground state while exiting the MMOT. The atoms travel in the magnetic guide to a detection region about 1.7 m away from the injection point. As shown by the overlay in Figure 1, a typical distribution of atoms in the detection region samples magnetic fields up to 50 G. Such fields result in Zeeman shifts on the order of 70 MHz, which exceed the linewidth of typical probe transitions, such as the Rb 5S$_{1/2}$ $\rightarrow$ 5P$_{3/2}$ transition (wavelength $\lambda = 780$ nm, linewidth $\Gamma/2\pi = 6$ MHz), by about a factor of ten. Because the device operates in a continuous manner (with the magnetic field always on), Zeeman shifts must be taken into account when analyzing fluorescence images of the atomic flow. In the following, it is described how the atomic density distribution can be measured using images obtained in the presence of these Zeeman shifts.

3 Closed-channel imaging

3.1 Continuous atomic-beam probing

To most readily observe the atomic beam, continuous re-pump and probe lasers are co-aligned such that they illuminate a small portion of the atomic flow. The re-pump laser, tuned to the $F = 1 \rightarrow F' = 2$ transition, optically pumps the guided atoms in the $|F = 1, m_{\mathrm{F}} = -1\rangle$ state into an $F = 2$ state. The re-pumped atoms generate abundant fluorescence from the probe laser, which is tuned on-resonance with the closed-channel $F = 2 \leftrightarrow F' = 3$ cycling transition. The fluorescence imaged onto a CCD camera enables continuous, spatially resolved, real-time atomic-beam observation (see Fig. 2, left image).

Continuous imaging of the atomic distribution has certain drawbacks. The radiative force from the probe laser accelerates atoms quickly out of resonance and causes a diminishing signal in the atomic beam direction. Further, due to re-pumping of the atoms into the $F = 2$ bright state and the subsequent closed-channel fluorescence on the $F = 2 \leftrightarrow F' = 3$ transition, a mixture of low- and high-magnetic-field seeking sub-levels is populated. The magnetic-dipole force in the guide is different for these various magnetic sub-levels. In addition, the atoms are exposed to the diffusive component of the radiative force due to the probe laser. Hence, the atomic flow is significantly diffused in a complicated manner during the imaging. Therefore, the observed image profile transverse to the atom flow is wider than the actual atomic distribution in the guide. The widening of the atomic-beam profile increases in the direction of the atomic flow. The fluorescence also diminishes in the direction of the atomic flow due to the reduction in the atomic density and the increase of both Doppler and Zeeman shifts. These effects lead to images of a broadened and distorted atomic-beam, as shown in the left panel of Figure 2.

3.2 Elimination of image distortion using a strobe technique

In order to obtain undistorted images of the atomic distribution, the re-pump and probe beams in the imaging region are pulsed. The duration of each strobe pulse is short enough such that particle motion during the strobe-pulse duration can be neglected. The waiting time between subsequent strobe pulses is chosen sufficiently long that each strobe pulse interacts with an entirely undisturbed section of guided atomic beam.

For ^{87}Rb, the scattering rate at saturation intensity (about 10^7 s^{-2}) corresponds to an average acceleration of 6×10^4 m/s^2 for atoms resonant with the probe light. Assuming that an atom starts from rest, its displacement during the 20 μs long detection pulse is $\leq$ 12 μm. Because this displacement is much smaller than the atomic-beam diameter (about 200 μm), atomic-motion-induced blurring can be neglected for strobed atomic-beam images. To obtain a high signal-to-noise ratio in the strobed fluorescence images, typically 1000 strobed images are accumulated (which takes only on the order of 1 second). The strength of the strobing technique becomes apparent by comparing the left (continuous) and right (strobed) panels of Figure 2. The strobed image is not blurred in the direction transverse to the atomic flow and extends in an unabated manner over the 500 μm length of the illuminated atomic-flow segment.

3.3 Influence of Zeeman effects

In a high-gradient magnetic guide such as ours, atoms are tuned out of resonance from the probe laser frequency at distances of only a few tens microns away from the guide axis. Due to the spatial variation of Zeeman shifts, the number of closed-channel probe photons scattered per atom varies in a complicated manner throughout the detection region. The spatial variation in the number of probe photons scattered per atom becomes even more significant because of the position-dependence of the probe-beam intensity, the position-dependence of the angle between laser polarization and magnetic field, and optical pumping among magnetic sublevels. Consequently, fluorescence images produced by a strobed, monochromatic, closed-channel probe laser differ strongly from the density profile of cold atoms in the magnetic guide. Thus, it is highly impractical to extract the atomic density profile from the measured closed-channel fluorescence images.

4 Open-channel imaging

4.1 Outline of the method

The difficulties described in Section 3 are circumvented by using an imaging method that produces a constant photon yield per atom, independent of atom location and detailed laser parameters. The method relies on the use of an open-channel transition to probe the atoms. In the present case, in which ^{87}Rb atoms are traveling in the $|F = 1, m_{\mathrm{F}} = -1\rangle$ state, the open-channel transition is the $F = 1 \rightarrow F' = 2$ re-pump transition. An atom in $F = 1$ scatters a re-pump photon and decays into one of the two hyper-fine ground levels $F = 1$ and $F = 2$. If the atom decays into the $F = 1$ level, the scattering process is repeated. If the atoms decays into the $F = 2$ level, it ceases to scatter more probe photons because the $F = 2 \rightarrow F' = 2$ transition is 6.83 GHz red-detuned from the re-pump transition. In Section 4.2, we find that, on average, an atom scatters 2.5 photons before being transferred into the non-resonant $F = 2$ state, independent of laser intensity and Zeeman shift. To ensure a uniform photon yield throughout the atomic sample, we only require the excitation rate on the open-channel re-pump transition $F = 1 \rightarrow F' = 2$ to be $\gtrsim$2.5 times the inverse imaging-pulse width ($\gtrsim 2.5 \times (20\ \mu\mathrm{s})^{-1} = 1.25 \times 10^5$ s^{-1} under the conditions of Fig. 2). Assuming an intensity of $10 I_{\mathrm{sat}}$, where $I_{\mathrm{sat}} = 1.6$ mW/cm^2 is the saturation intensity, this condition is satisfied well for magnetic fields up to at least $\sim$60 G. If the atomic distribution samples magnetic fields less than this value, as in Figure 2, almost all atoms will have sufficient time to become optically pumped into the non-resonant $F = 2$ state during their interaction with the open-channel imaging pulse. Consequently, the photon yield per atom will be uniform throughout the atomic sample, and the fluorescence images will be proportional to the atomic distribution projected onto the image plane. The only disadvantage of this method is that the average yield of 2.5 photons per atom is quite low. Hence, a sensitive camera is required to acquire the open-channel images.

4.2 Simulation

We have simulated the open-channel detection process of cold ^{87}Rb atoms in the $|F = 1, m_{\mathrm{F}} = -1\rangle$ state in the magnetic field generated by two parallel wires carrying parallel currents of 300 A (as in Fig. 1). Using the quantum Monte-Carlo wave function (QMCWF) technique [15], we simulate the time evolution of the atoms in a laser field detuned by -15 MHz from the $F = 1 \rightarrow F = 2$ open-channel probe transition, corresponding to the experimental conditions. In the simulation, we include the ground state hyperfine levels $F = 1$ and $F = 2$ and the excited-state levels $F' = 0$, 1, and 2. The exact magnetic field of appropriately placed line currents extending in the z-direction is used, resulting in a transverse gradient of 2.7 kG/cm in the vicinity of the minimum of the magnetic-field strength, as shown in Figure 1. Zeeman shifts are assumed to be linear throughout the detection region. For the ground-state manifold ($F = 1$, g-factor $g_{\mathrm{F}} = -1/2$), this approximation is very well satisfied due to the large hyperfine splitting (6.83 GHz) between $F = 1$ and $F = 2$. The coupled excited-state manifolds ($F' = 0$, 1, and 2 with $g_{\mathrm{F}'} = 2/3$) have rather small separations (72 MHz between 0 and 1, and 157 MHz between 1 and 2). Consequently, in the magnetic-field range $B \lesssim 60$ G occupied by the atoms (see Fig. 1) the Zeeman shifts of some excited-state sublevels exhibit deviations up to about 40 MHz from linearity [16]. While in our simulation we neglect these nonlinearities, we believe that our simulation results are qualitatively valid because most Zeeman components of the open-channel probe transition are quite far-off-resonant anyways. As in the experiment, the polarization of the simulated open-channel imaging beam is linear, transverse to the guide wires, and in the plane spanned by the guide wires. The temperature of the guided atomic beam is low enough that Doppler shifts ($\lesssim$1 MHz) are entirely negligible.

In the simulation, we average 500 quantum trajectories at each point on a uniform grid in a plane transverse to the line currents within the detection region. Each quantum trajectory is propagated until the atom is transferred from the $F = 1$ into the $F = 2$ sub-level, or until the simulation time reaches the end of the 20 μs imaging pulse. During the imaging pulse, the atoms are assumed to be stationary. The observables of primary interest are the average photon yield per atom and the probability that an atom is transferred into the $F = 2$ state, each as a function of position.

The results show that, for a sufficiently intense probe, atoms become transferred into the $F = 2$ state with near 100% probability, as can be seen in the right panel of Figure 3. In a crude approximation, one may assume that in the simulated open-channel detection process the atoms are predominantly excited into the $F' = 2$ level. By summing over the transition probabilities, one can see that the decay probabilities from $F' = 2$ state into the ground hyperfine levels $F = 1$ and $F = 2$ are 50% each. Thus, neglecting off-resonant excitation into the $F' = 1$ and $F' = 0$ levels, the probability $P(n)$ that an atom scatters n photons while being transferred into the $F = 2$ ground state is $P(n) = 2^{-n}$. The average photon number then is expected to be $\langle n \rangle = \sum_{n=1}^{\infty} nP(n) = 2$.

However, the results from the simulation show that, for magnetic field magnitude $\gtrsim$30 G, the average number of photons required to optically pump atoms into the $F = 2$ ground state is > 2. This can be explained as follows. For higher magnetic field values, the magnetic subcomponents of the $F = 1 \rightarrow F' = 2$ transition tune out of resonance due to Zeeman shifts, and photon scattering due to the $F = 1 \rightarrow F' = 1$ transition becomes more significant. The probability that an atom excited into the $F' = 1$ level decays back into the $F = 1$ ground state is 5 times greater than that of decaying into the $F = 2$ ground state. Thus, for higher magnetic fields, as the $F = 1 \rightarrow F' = 1$ transition becomes more important, an atom scatters more photons before becoming optically pumped into the $F = 2$ ground state. The simulation results shown in Figure 4 indicate that for an atomic beam of $\sim$200 μm diameter and $I = 20I_{\mathrm{sat}}$, each atom scatters on average 2.5 photons, with a variation <0.5 photons. Under these conditions, almost all atoms are optically pumped into the $F = 2$ ground state, as shown in the right panel of Figure 3.

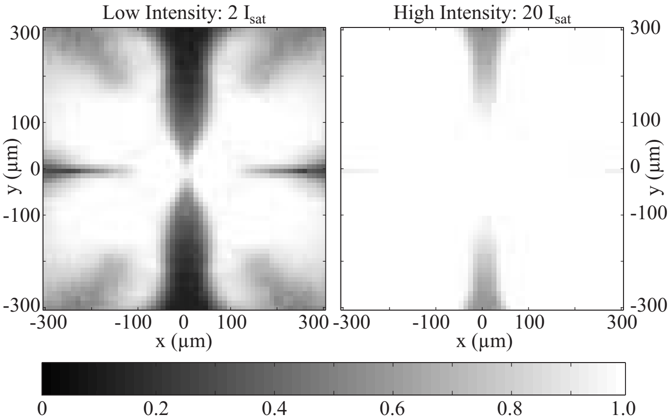

Fig. 3. Probability that an atom is transferred into the $F = 2$ state during the 20 μs open-channel imaging pulse vs. position (x, y), for probe intensities $2I_{\mathrm{sat}}$ (left) and $20I_{\mathrm{sat}}$ (right). The probe laser propagates along the y-direction, is linearly polarized in x-direction, and is detuned by -15 MHz from the $F = 1 \rightarrow F = 2$ transition. In the high-intensity case, it is apparent that nearly 100% transfer is achieved throughout the displayed spatial range.

It is apparent in Figures 3 and 4 that low illumination intensity results in a strong position dependence of the transfer efficiency and photon yield, respectively. The radial dependence is largely due to the increase of the Zeeman shift as a function of radial position in the magnetic guide. The structures present in the angular degree of freedom reflect the fact that the angle between laser polarization and the magnetic field varies throughout the detection region. This leads to variations in the relative importance of π, σ^+ and σ^- transitions and in optical pumping among the magnetic sublevels of $F = 1$.

Overall, the QMCWF simulations verify that for a sufficiently high probe intensity the open-channel imaging technique yields a nearly uniform number of photons per atom throughout the probe region. For trap-field-induced shifts of the open-channel probe transition $\lesssim$100 MHz and an imaging-pulse duration of 20 μs, the simulations show

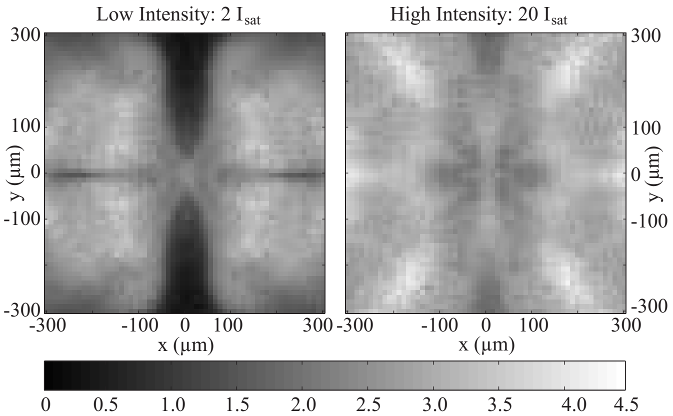

Fig. 4. Simulated average number of photons $N_{\mathrm{P}}(x, y)$ vs. position (x, y), scattered by magnetically trapped Rb atoms illuminated by an open-channel imaging pulse of 20 μs duration and a constant intensity of $2I_{\mathrm{sat}}$ (left) and $20I_{\mathrm{sat}}$ (right). The probe laser parameters are the same as in Figure 3. Denoting the atomic volume density distribution $n_{\mathrm{A}}(x, y)$, the experimental fluorescence profiles seen in the overlay of Figures 1 and 7 below correspond to the integral $\int N_{\mathrm{P}}(x, y) n_{\mathrm{A}}(x, y) dy$.

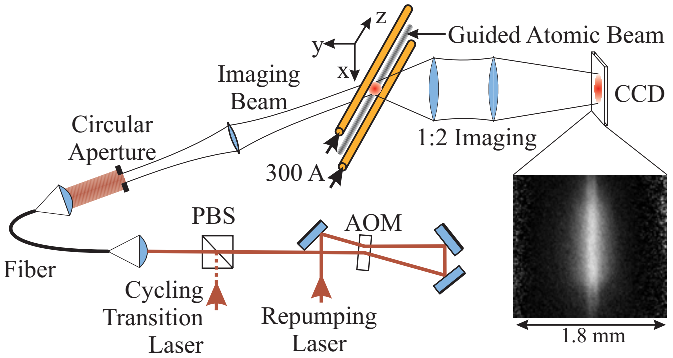

Fig. 5. (Color online) Imaging setup. The imaging light first passes through an acousto-optic modulator (AOM) which provides fast switching for the imaging pulse. The pulsed imaging light is then passed through a fiber, collimated, and directed onto an aperture of ≈1 mm diameter. By imaging the aperture into the probe region of the magnetic guide, an approximate top-hat intensity profile of the imaging beam is achieved. The imaging beam is polarized along the x-axis. Each probe pulse optically pumps the atoms from $F = 1$ into $F = 2$, thereby generating ≈2.5 photons per atom. This open-channel fluorescence is observed using a lens system that images the guided atomic beam onto a sensitive CCD camera with a 1:2 magnification ratio.

that an imaging-pulse intensity of $10I_{\mathrm{sat}}$ is sufficient to achieve a uniform photon yield.

4.3 Imaging setup

The utilized imaging setup is shown in Figure 5. A laser locked 15 MHz below the $F = 1 \rightarrow F' = 2$ transition provides both re-pumping light for laser-cooling as well as the open-channel probe light for imaging of the magnetically guided atoms. An acousto-optic modulator (AOM) in a double-pass configuration allows for fast switching of the imaging pulse. The probe beam is aligned through the AOM such that its frequency is not shifted during its on-phase, while a complete extinction is achieved during its off-phase (see bow-tie beam path through AOM in Fig. 5). The time interval between adjacent imaging pulses is chosen sufficiently long that each imaging pulse interacts with a completely undisturbed sample of the atomic beam. For the results presented here, 20 μs detection pulses are followed by waiting intervals ranging from 1 ms at low imaging-beam intensity to 4 ms at high intensity. The output of the AOM is passed through a single mode fiber and collimated to obtain a clean spatial Gaussian mode of about 5 mm diameter. This beam is then used to illuminate an aperture ≈1 mm in diameter. This filtering technique creates an approximate top-hat intensity profile immediately after the aperture. By imaging the plane of the aperture directly into the atomic beam, as indicated in Figure 5, the intensity profile of the probe beam in the detection region also represents a top-hat profile, with minimal diffraction effects. Two benefits of this illumination method are that the intensity throughout the detection region is uniform and that scattering of probe light on the guide wires is minimized.

Because one probe pulse yields only ≈2.5 photons per atom emitted over a solid angle of 4π steradians, and because there are only about 9000 atoms in the probe volume, an efficient imaging of the atomic fluorescence is critical. The imaging system consists of two 2-inch diameter achromatic lenses with an object-side numerical aperture of 0.3 and magnification factor of 2. We further use a back-illuminated CCD (quantum efficiency ≈75% at 780 nm) from Andor Technology to detect the atomic fluorescence (Part number iXon DV-887 ECS BV). This CCD has an on-chip charge-amplifying gain element that enables near-single-photon detection capability.

4.4 Open-channel imaging results

In Figure 6 we show a comparison between atomic-beam fluorescence profiles measured using either a closed-channel image or an open-channel image. The profiles are obtained by integrating images such as the ones shown in Figure 2 along the atomic-beam direction, defined to be the z-axis (vertical axis in Fig. 2). In order to eliminate the influence of diffraction effects and of the circular shape of the illumination region on the beam profiles, the integration range is limited to a region in which the measured fluorescence does not significantly depend on z. While the closed-channel measurement in Figure 6 has a high signal strength and a high signal-to-noise ratio, it does not reflect the true atomic distribution, as explained in Section 3.3. The open-channel profile in Figure 6 reveals that the atomic-beam density profile is significantly wider than suggested by the closed-channel profile. Thus, Figure 6 shows the advantages of using images obtained with an open-channel probe over those obtained with a closed-channel probe for determining atomic distributions. In the

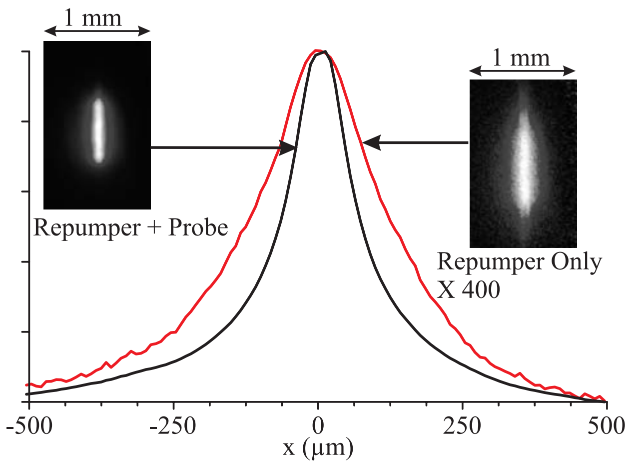

Fig. 6. (Color online) (Top curve) Fluorescence profile of a magnetically guided beam of cold atoms obtained by open-channel ($F = 1 \rightarrow F' = 2$) fluorescence imaging using probe intensity of $5I_{\mathrm{sat}}$. (Bottom curve) Corresponding fluorescence profile obtained by measuring fluorescence from the closed-channel $F = 2 \leftrightarrow F' = 3$ cycling transition.

following, we demonstrate experimentally that for sufficiently high probe intensity, open-channel imaging provides fluorescence images that are approximately proportional to the underlying atomic-beam density profiles.

The open-channel fluorescence images displayed in the insets on the right of Figures 5 and 6 are background-subtracted, discrete, pixelated images $N_{\mathrm{pix}}(i, k)$. The corresponding area densities of atoms in the xz-object plane are obtained from

$$n_{\mathrm{A,area}}(x, z) = \eta N_{\mathrm{pix}}(i, k) \tag{1}$$

where (x, z) are the object-plane coordinates that correspond to the discrete image-plane pixel coordinates (i, k). The factor η is given by:

$$\eta = \frac{1}{2.5}\frac{1}{N_{\mathrm{shot}}}\frac{1}{\eta_{\mathrm{ccd}}}\frac{4\pi}{\Omega_{\mathrm{lens}}}\frac{1}{A}. \tag{2}$$

There, the factor 1/2.5 accounts for the fact that each atom is assumed to scatter 2.5 photons, N_{shot} is the number of strobe pulses that have contributed to the image, η_{ccd} is the pixel count the CCD produces per single photon passing through the camera lens, Ω_{lens} is the solid angle subtended by the lens aperture from the location of the atoms, and A is the object-plane area that corresponds to one camera pixel (A equals the CCD-pixel area divided by the square of the imaging magnification factor). The values of η_{ccd} and Ω_{lens} have been measured using several calibration setups. The apparent number of atoms in the detection volume per length in x-direction, $n_{\mathrm{lin}}(x)$, computed under the assumption that each atom has scattered 2.5 photons during the imaging pulse, is then given by

$$n_{\mathrm{lin}}(x) = \int_0^{L_z} n_{\mathrm{A,area}}(x, z)dz, \tag{3}$$

where the range of the z-integration, L_z, is given by the extent of the probe light in the z-direction.

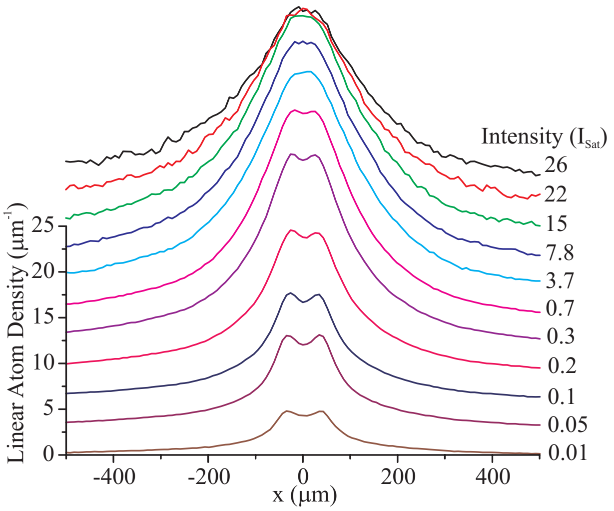

Fig. 7. (Color online) The linear density of detected atoms $n_{\mathrm{lin}}(x)$ derived from fluorescence images obtained with the indicated intensities of the open-channel imaging laser. For clarity, the curves are offset from each other by a constant amount. With increasing intensity, the profile converges towards the atomic density distribution. At high intensity, the noise level increases due to an increasing amount of probe-beam stray light from the vacuum windows and guide wires (the stray light scales linearly in intensity). Atoms upstream of the detection region in the guide also scatter probe-beam stray light, leading to an atom loss that scales linearly in probe intensity. This loss becomes noticeable at probe intensities $\gtrsim 15I_{\mathrm{sat}}$.

In Figure 7, we show apparent linear atom densities $n_{\mathrm{lin}}(x)$ for different imaging-laser intensities. For the apparent linear atom density $n_{\mathrm{lin}}(x)$ to represent the actual linear atom density, the open-channel imaging pulse must be sufficiently intense that $\gamma_{\mathrm{s}}\tau \gtrsim 2.5$ throughout the atomic sample, where γ_{s} is the photon scattering rate on the open-channel transition and τ is the duration of the detection pulse. Under that condition, almost all atoms in the detection region are transferred into the $F = 2$ state during the probe pulses, and the photon yield per atom uniformly equals $\approx$2.5 photons per atom. At too low probe intensity, the atoms are under-counted because the average photon yield per atom is $<$2.5. The data shown in Figure 7 demonstrates that with increasing probe intensity the apparent linear atom density actually converges to an intensity-independent result, which approximately reflects the true linear atom density. In Figure 7, the displayed profiles show the true linear atom density for intensities $I \gtrsim 5I_{\mathrm{sat}}$.

In the measurement shown in Figure 7, the open-channel imaging laser was slightly detuned from the $F = 1 \rightarrow F' = 2$ atomic resonance for technical reasons. This detuning causes the open-channel imaging laser light to be resonant with an $F = 1 \rightarrow F' = 2$ transition at a distance of approximately 30 μm from the center of the trap. At low intensity, the non-uniform scattering behavior (see left panel of Fig. 4, where the probe detuning is taken into account) results in a double-peak structure in the fluorescence profiles, as can be seen in Figure 7 for $I \lesssim 1I_{\mathrm{sat}}$.

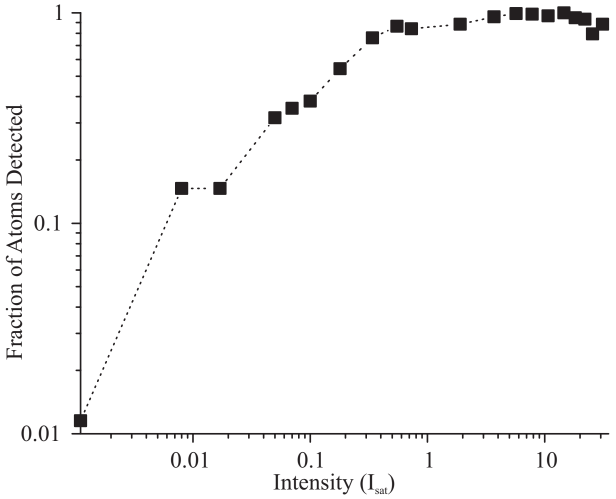

Fig. 8. Fraction of detected atoms as a function of the intensity of the open-channel imaging pulse. The data are obtained by integrating the curves in Figure 7 and by normalizing with the result obtained in the high-intensity limit (which corresponds to 9000 atoms). The slight decrease observed at intensities beyond $I \gtrsim 15 I_{\text{sat}}$ is due to the probe-light scattering mentioned in the caption of Figure 7.

As the imaging-beam intensity and thus the scattering rate γ_{s} increase, the double-peak structure disappears, while the apparent linear atom density distribution converges towards the actual one.

The apparent numbers of atoms in the detection volume for different open-channel probe intensities are calculated by integrating the profiles in Figure 7. In Figure 8 we show the detected fraction of atoms, i.e. the ratio of the apparent number of atoms calculated at a given open-channel probe intensity to the number of atoms calculated in the limit of high probe intensity. As shown in Figure 8, the detected fraction of atoms increases as the intensity of the probe pulse is increased. The detected fraction saturates around $5I_{\text{sat}}$, indicating that under this condition all atoms become optically pumped from the $F = 1$ to the $F = 2$ ground state and deliver, on average, 2.5 photons each. Figure 8 exhibits a plateau region extending from $5I_{\text{sat}}$ upward. On the plateau, the open-channel imaging is fully effective throughout the probe volume. We find that the plateau corresponds to 9000 atoms present in the detection volume. For the data in Figure 8 the length of the illumination region was $L_{\text{z}} = 690$ μm, and the atomic-flow velocity $v_{\text{z}} = 1.8$ m/s (measured with a time-of-flight method). Thus, the atom flux in the guide is $9000 \times (v_{\text{z}}/L_{\text{z}}) = 2.3 \times 10^7$ atoms s^{-1}, as reported in [6].

5 Conclusion

We have characterized an open-channel detection technique for measuring atomic distributions in high-gradient magnetic traps. This technique does not require the trapping field to be switched off and therefore is most useful for static-field traps. This technique is easy to implement in any existing imaging setup and can be generalized to traps that involve both electric and magnetic fields, as well as AC electric-dipole traps (far-off-resonant laser traps).

This work was supported by the Army Research Office and the Office of Naval Research (Project number 42791-PH).

References

1. W.D. Phillips, P.L. Gould, P.D. Lett, Science **239**, 877 (1988), and references therein
2. J.M. Doyle, B. Friedrich, Nature **401**, 750 (1999)
3. M. Fauquembergue et al., preprint: `arXiv:cond-mat/0507129` v2 (2005)
4. M. Vengalattore, R.S. Conroy, W. Rooijakkers, M. Prentiss, J. Appl. Phys. **95**, 4404 (2004)
5. W. Hänsel, J. Reichel, P. Hommelhoff, T.W. Hänsch, Phys. Rev. Lett. **86**, 608 (2001)
6. S.E. Olson, R.R. Mhaskar, G. Raithel, Phys. Rev. A **73**, 33622 (2006)
7. T. Lahaye et al., Phys. Rev. A **72**, 33411 (2005)
8. P.O. Schmidt et al., J. Opt. B: Quant. Semiclass. Opt. **5**, 170 (2003)
9. K.E. Gibble, S. Kasapi, S. Chu, Opt. Lett. **17**, 526 (1992)
10. J. Schuster, *Stolawinen in einem Bose-Einstein-Kondensat*, Ph.D. thesis, Universität Konstanz, 2002
11. K.I. Lee, J.A. Kim, H.R. Noh, W. Jhe, Opt. Lett. **21**, 1177 (1996)
12. R.S. Williamson III, P.A. Voytas, R.T. Newell, T. Walker, Opt. Exp. **3**, 111 (1998)
13. S. Weyers, E. Aucouturier, C. Valentin, N. Dimarcq, Opt. Commun. **143**, 30 (1997)
14. P. Cren, C.F. Roos, A. Aclan, J. Dalibard, D. Guéry-Odelin, Eur. Phys. J. D **20**, 107 (2002)
15. R. Dum, P. Zoller, H. Ritsch, Phys. Rev. A **45**, 4879 (1992)
16. D.A. Steck, *Rubidium 87 D Line Data*, LA-UR-03-8638, Los Alamos Nat. Lab. (2003)